

Discrete-Time Modelling of Li-ion Batteries with Electrochemical Overpotentials Including Diffusion

Alan G. Li^a, Karthik Mayilvahanan^b, Alan C. West^b, Matthias Preindl^{a,*}

^a*Department of Electrical Engineering, Columbia University in the City of New York, 500 W. 120th St., Mudd 1310, New York, NY, 10027, USA*

^b*Department of Chemical Engineering, Columbia University in the City of New York, 500 W. 120th St., Mudd 801, New York, NY, 10027, USA*

Abstract

A battery equivalent circuit model (ECM) is proposed using a novel physics-based diffusion component and N resistor-capacitor (RC) pairs, hence its name the ‘DNRC model’. The DNRC model characterizes ohmic, charge transfer, and diffusion overpotentials in the time domain with physically-meaningful circuit elements. Unlike the Warburg impedance, the diffusion component has no need for frequency-domain data and is formulated entirely in the time domain. Physical interpretability is validated by comparison with physics-based model (PBM) generated data. Experimental validation is performed at a wide range of state of charge (SoC) and state of health (SoH) using pulse injection and drive cycle data. The mean absolute percent error is below 0.3% using 5 circuit elements for 4 minutes of an arbitrary current load. The DNRC model is grounded in physical principles, suitable for real-time estimation, and may form the basis for new approaches to degradation reduction or diagnosis in battery management systems.

Keywords: Lithium batteries, Equivalent Circuit Model, Electrochemical overpotentials

1. Introduction

Lithium-ion batteries (LIB) are becoming increasingly popular for energy storage in applications such as electric vehicles [1]. LIB systems are typically controlled with a battery management system (BMS), which monitors and estimates the cell states to ensure safe and efficient operation. Knowledge of states such as state of charge (SoC) and state of health (SoH) is crucial for reliability, and can also inform more effective BMS protocols to increase pack power output and useful lifetime [2, 3, 4]. In most LIB systems, temperature, current, and voltage are the only measurements available. This means that there is no direct knowledge of how the cells’ internal chemistry changes with degradation or usage. Battery models therefore form the basis of most conventional BMS, and are used for state estimation [5]. Models

must use limited observations to deduce changes in the battery system. There are three types of models: physics-based models (PBM), equivalent circuit models (ECM), and data-driven models.

Broadly, there are 4 criteria for models: generality, accuracy, interpretability, and speed. Models with high generality can easily adapt to different cell chemistries. Accuracy refers to the voltage tracking from inputs such as current and temperature. Interpretable models have parameters that are highly correlated with internal cell parameters, and are thus particularly useful for tracking degradation in cells. Understanding how a cell degrades as a function of usage is important for optimizing performance and increasing useful lifetime [6, 7]. For real-time use, models with fast parameter identification and voltage prediction are desired.

PBM are derived directly from physical principles governing the electrochemical processes occurring in battery cells. Due to the complexity of battery cells, PBM are typically composed of more than 50 parameters, which may not be known in non-laboratory environments, and are governed by nu-

*Corresponding author.

Email address: matthias.preindl@columbia.edu
(Matthias Preindl)

merous coupled partial differential equations. This makes PBM estimation very time-consuming. PBM are very accurate, however, and the parameters are fully interpretable because they are linked directly to the cell structure and chemistry. Because of this, PBM can be used to gain insight to degradation processes in the cell. Reduced-order PBM have attracted attention for their faster estimation time [8, 9, 10], but still require knowledge of internal cell parameters, making the models difficult to generalize for different cell chemistries.

Conventional ECM are typically composed of an ideal voltage source connected to passive circuit elements such as resistors and capacitors. The N^{th} order RC-pair (NRC) model is commonly used, shown in Figure 1b, where V_{OC} represents the open-circuit voltage (OCV) of the cell and V_o is terminal voltage. Resistance R_0 represents the ohmic resistance of the cell. Each RC-pair has a characteristic time-constant to capture time-varying phenomena in the cell. Since an infinite number of RC-pairs can be included in the model, the output voltage prediction accuracy is very high, and can be applied to any cell chemistry. ECM parameters can be estimated and simulated very quickly. ECM, however, suffer from poor interpretability. When several RC-pairs are included in the model, the numerous circuit elements have little to no physical meaning. This means that a highly-accurate ECM may not yield any information on the internal cell parameters.

Data-driven models are not as widely used as PBM or ECM, but have potential to provide highly fast and accurate predictions [11, 12]. Data-driven methods include neural networks or support vector machines, which can model complex systems when trained and validated with large datasets. They have no interpretability, and are considered black-box systems.

Real-time battery models typically use time-domain data, but the frequency domain offers another perspective in the form of electrochemical impedance spectroscopy (EIS). EIS is a popular laboratory technique for analyzing cell states and degradation [13, 14, 15]. This is partially because of its ability to capture electrochemical processes using a simple ECM such as the Randles circuit [16], shown in Figure 1c, where W refers to the Warburg impedance and Warburg coefficient A_W . Whilst electrochemically-based ECM like the Randles circuit do not represent internal cell parameters, they are interpretable, and can offer insight into internal processes such as diffusion.

EIS is a time-consuming but valuable technique for insight into internal cell processes. Thus several studies have pursued fast time-domain identification of circuit models typically formulated in the frequency domain [17, 18, 19, 20, 21, 22]. In [17, 18, 19], fractional-order system identification methods are presented. Fractional-order systems refer to the common-phase element (CPE), which yields a fractional order transfer-function. This has been shown to accurately model LIB behavior [23]. CPE models are a promising basis for state estimation and degradation analysis [19], but face challenges in system order identification due to its variation with cell states. In [20, 21, 22], physically-meaningful ECM are formulated. These ECM include a unique time-domain description of diffusion derived from physical principles. While promising, the models face challenges in accuracy and interpretability.

1.1. Contributions and Outline

This article proposes a new general-purpose ECM, named the DNRC model, that captures electrochemical overpotentials including diffusion in the time domain. A novel diffusion element is derived from physics-based principles. The model is formulated in discrete-time, allowing for fast estimation. The DNRC model therefore increases the physical interpretability of conventional ECMs without sacrificing accuracy or speed.

Model validation is performed using three distinct datasets: (1) Simulated pulse data using a PBM, (2) Experimental pulse injection data for a wide range of SoC and SoH, and (3) Experimental drive cycle data. The simulated data demonstrates the ability of the DNRC model to capture and isolate the effects of internal cell states such as diffusivity, reaction constant, and contact resistance. The experimental data demonstrates that the proposed model is general-purpose, accurate, and fast.

In Section 2, the model is formulated and derived. In Section 3, data processing is described. The simulated and experimental datasets are analyzed and discussed in Sections 4 and Section 5. The article is then concluded in Section 6.

2. Model description

The proposed model is represented in Figure 1a, with output voltage V_o given by

$$V_o(t) = V_{OC}(t) - V_s(t) - V_{ct}(t) - V_D(t) \quad (1)$$

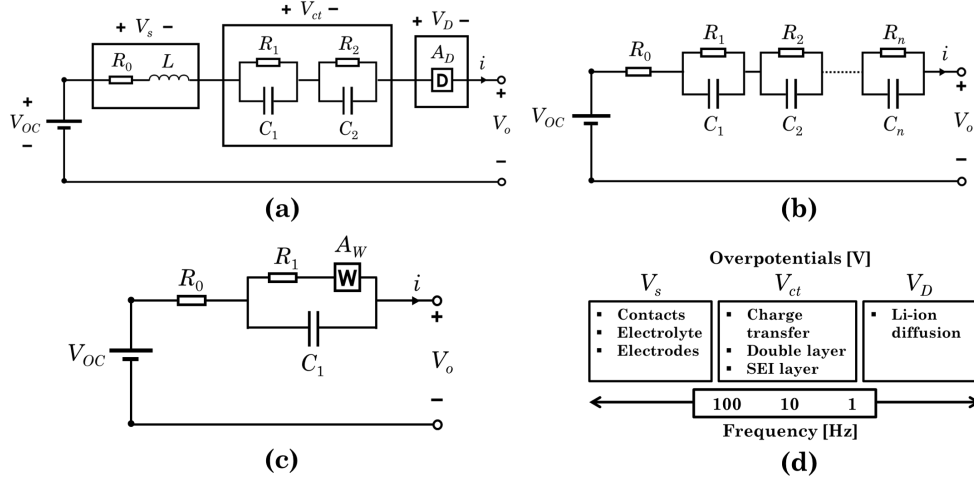


Figure 1: Comparison between the proposed and commonly-used equivalent circuit models, with (a) Proposed D2RC circuit model, (b) N^{th} order RC-pair circuit model, (c) Randles circuit model for electrochemical impedance spectroscopy, and (d) Summary diagram of electrochemical overpotentials and characteristic frequencies

where V_{OC} is the OCV, and V_s , V_{ct} , and V_D are the solution, charge transfer, and diffusion overpotentials. The model is referred to as the DNRC model because it combines the elements of a conventional NRC model with a newly-proposed diffusion element. It is renamed after the number of RC-pairs included, e.g., D1RC for 1 pair or D2RC for 2 pairs. Each labelled voltage is linked to an electrochemical overpotential, and each is described in this section. A summary diagram of the overpotentials is presented in Figure 1d. The discrete-time expression is formulated using sampling interval Δt and time step t_k , with initial conditions from rest.

2.1. Open-circuit voltage

The OCV, represented is the terminal voltage of the battery cell V_o after sufficient rest. The OCV is known to vary significantly with SoC and slightly with SoH. OCV is estimated directly from the cell current, with no fitting parameters. There are many approaches to OCV estimation, as detailed in [24, 25, 26]. In this article, V_{OC} is obtained with a simple recursive definition,

$$V_{OC}(t_{k+1}) = \left(\frac{\partial V_{OC}}{\partial \text{SoC}} \Big|_{\text{SoC}(t_k)} \right) \frac{i(t_k)\eta\Delta t}{Q_m} + V_{OC}(t_k) \quad (2)$$

where $\frac{\partial V_{OC}}{\partial \text{SoC}}$ is calculated offline, i is the cell current, η is the coulombic efficiency, $\Delta t = t_{k+1} - t_k$ is the sampling interval, and Q_m is the maximum capacity of the cell.

2.2. Solution overpotential

The solution overpotential, represented by V_s , is the ohmic voltage developed across the electrodes, electrolyte, and contacts. Typically V_s captures high-frequency behavior in the cell above 100 Hz. It is modelled using a resistor and an inductor, and governed by the equation

$$V_s(t) = R_0 i(t) + L \frac{di}{dt} \quad (3)$$

where $i(t)$ is the cell current, R_0 is a series resistance, and L is an inductor.

Using zero-order hold (ZOH) discretization, we have

$$V_s(t_{k+1}) = \frac{R_0 \left(i(t_{k+1}) - i(t_k) e^{-\frac{\Delta t R_0}{L}} \right)}{1 - e^{-\frac{\Delta t R_0}{L}}} \quad (4)$$

Note that it is inappropriate to include the inductor when the data sampling frequency is below 100 Hz. This is because its effects are not observed at lower sampling frequencies. When this is the case, we approximate $L \rightarrow 0$, so we have

$$V_s(t_k) = R_0 i(t_k) \quad (5)$$

2.3. Charge-transfer overpotential

The charge-transfer overpotential, represented by V_{ct} , models overpotentials from multiple phenomena in the cell that act from 1 to 100 Hz. The RC-pairs are related to the double-layer capacitance

and charge migration at the electrodes and at the solid-electrolyte interphase (SEI) layer. Each RC-pair is governed by the equation

$$i(t) = i_{Rn}(t) + R_n C_n \frac{di_{Rn}}{dt} \quad (6)$$

where i_{Rn} is the current through the resistor R_n , and C_n is the capacitance.

Using ZOH, the discrete-time form is given by

$$i_{Rn}(t_{k+1}) = i_{Rn}(t_k) e^{-\frac{\Delta t}{R_n C_n}} + i(t_k) \left(1 - e^{-\frac{\Delta t}{R_n C_n}}\right) \quad (7)$$

Thus voltage V_{ct} is given by

$$V_{ct}(t_k) = \sum_{n=1}^N R_n i_{Rn}(t_k) \quad (8)$$

where $N = 2$ for the D2RC model. Note that V_s and V_{ct} are the basis of conventional NRC models.

2.4. Diffusion overpotential

The diffusion overpotential V_D models the voltage generated by the transport of Li-ions from concentration gradients in the cell, which is observed at low frequencies under 1 Hz. Stress-induced diffusion, though important, is assumed to be negligible compared to concentration gradients [27, 28]. Voltage V_D is derived assuming semi-infinite diffusion for a solid electrode [29]. Electrode structure effects are not considered. Fick's law for diffusion is then given by

$$\frac{\partial c_s}{\partial t} = \frac{D}{x} \frac{\partial}{\partial x} \left(x^2 \frac{\partial c_s}{\partial x} \right) \quad (9)$$

where c_s and D are the concentration and diffusion coefficient of lithium in the active material and x is a length vector across the electrode. Note that $x = 0$ represents the electrolyte-electrode interface and $x = L$ represents the electrode-collector interface.

We first consider diffusion overpotential from a single current step. Using the conditions

$$\begin{aligned} c_s(x, t = 0) &= c_{s,0} \\ \frac{\partial c_s}{\partial x} \Big|_{x=L} &= 0 \\ D \frac{\partial c_s}{\partial x} \Big|_{x=0} &= \frac{\Delta I}{q_e S} \end{aligned} \quad (10)$$

and assuming that $t_D \ll \frac{L^2}{D}$, it is shown in [29] that

$$\frac{dc_s(x=0, t)}{d\sqrt{t}} = \frac{2\Delta I}{q_e S \sqrt{D\pi}} \quad (11)$$

governs behavior over a single current step, where $c_{s,0}$ is the initial concentration, assumed constant across the electrode, ΔI is the value of the current step, t_D is the step duration, S is the active surface area of the electrode, and q_e is the elementary charge. Concentration is proportional to change in the relative stoichiometry of lithium in the electrode δ ,

$$dc_s = \frac{N_A}{v_M} d\delta \quad (12)$$

which is then used to obtain the diffusion overpotential η_D using

$$\frac{d\eta_D}{d\sqrt{t}} \frac{d\delta}{d\eta_D} = \frac{2\Delta I v_M}{SF\sqrt{D\pi}} \quad (13)$$

where v_M is the molar volume of active material, F is Faraday's constant, and N_A is Avogadro's number. It can be shown that

$$\frac{d\eta_D}{d\delta} = \beta \frac{\partial V_{OC}}{\partial SoC} \quad (14)$$

where $\frac{d\eta_D}{d\delta}$ quantifies the change in overpotential due to the the amount of stoichiometric added lithium, $\frac{\partial V_{OC}}{\partial SoC}$ is the derivative of the OCV-SoC curve, and β is a conversion factor. Thus the variation of diffusion overpotential over time from a single current step is given by

$$\begin{aligned} \frac{d\eta_D}{d\sqrt{t}} &= \frac{2\beta\Delta I v_M}{SF\sqrt{D\pi}} \frac{\partial V_{OC}}{\partial SoC} \\ \eta_D &= \left(\frac{2\beta\Delta I v_M}{SF\sqrt{D\pi}} \frac{\partial V_{OC}}{\partial SoC} \right) \sqrt{t} \end{aligned} \quad (15)$$

Defining

$$A_D = \frac{2\beta v_M}{SF\sqrt{D\pi}} \quad (16)$$

we thus have

$$\eta_D = A_D \Delta I \left(\frac{\partial V_{OC}}{\partial SoC} \right) \sqrt{t} \quad (17)$$

where A_D is a diffusion-related constant for the cell at steady state.

To generalize this relationship for any number of current steps N_p , we introduce a diffusion state function $\psi_n(t)$ for the n^{th} step change, given by

$$\psi_n(t) = \Delta I_n \left(\frac{\partial V_{OC}}{\partial SoC} \Big|_{SoC(t_n)} \right) \sqrt{t - t_n} \quad (18)$$

where ΔI_n is the value of the step change, t_n is the time of the step change, and $t \geq t_n$. The overall

diffusion voltage is given by the superposition of all $\psi_n(t)$,

$$V_D(t) = A_D \sum_{n=1}^{N_p} \psi_n(t) \quad (19)$$

This shows that the voltage response at any time is composed of the superposition of all diffusion states from previous current steps.

For discretization, we consider the derivative

$$\frac{d\sqrt{t-t_n}}{dt} = \frac{1}{2\sqrt{t-t_n}} \quad (20)$$

By ZOH conditions, the discrete-time function is therefore given by

$$\psi_n(t_{k+1}) = \Delta I_n \left(\frac{\partial V_{OC}}{\partial SoC} \Big|_{SoC(t_n)} \right) \sqrt{H(t_k - t_n)(\Delta t + \psi_n^2(t_k))} \quad (21)$$

where H is the Heaviside step function.

2.5. Relation to EIS

The D2RC model bears notable similarities to the Randles circuit in Figure 1b. The impedance of W is given by

$$\frac{V_w(s)}{I_w(s)} = \frac{A_W}{\sqrt{s}} \quad (22)$$

where V_w is the voltage across W , I_w is current through W , $s = j\omega$ and ω is the angular frequency. The inverse Laplace transform suggests that the impedance is defined by a square-root characteristic with time. This is a specific case of a more generic fractional-order impedance.

For the proposed diffusion element, the square-root-of-time characteristic is exhibited by the voltage, rather than the impedance. This simplifies analysis because diffusion is no longer directly coupled with current.

3. Data Processing

3.1. Initial processing

As discussed in Section 2, there are two initial processing steps for OCV and the diffusion states. The derivative $\frac{\partial V_{OC}}{\partial SoC}$ is calculated off-line using pseudo-OCV data, obtained using a 0.1 C-rate discharge from 100 to 0% SoC. This is then used in equation 2. The OCV is initialized with the cell voltage after a rest period. In practice, since it is not always possible to rest the cell, methods such as Kalman filters can be used [26].

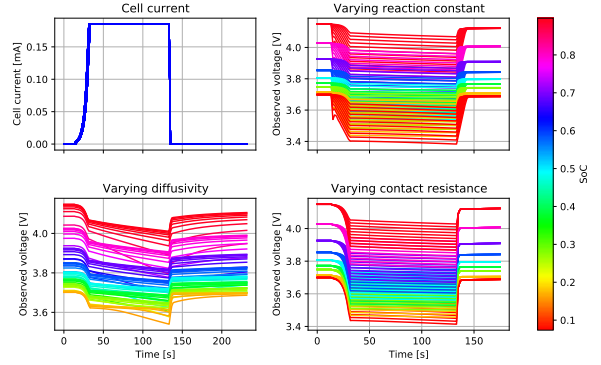


Figure 2: Cell current and output voltage of simulated datasets

To obtain the diffusion voltage as shown in equation 21, step change times t_n and step change values ΔI_n must be calculated from the cell current. A new current step is defined when the observed cell current changes by more than a small threshold I_{thr} over a single sampling interval. This is represented by the conditions

$$\begin{aligned} &\text{if } \left\{ |I(t_k) - I(t_{k-1})| > I_{thr} \right. \\ &\text{then } \left\{ \begin{aligned} t_n &= t_k \\ \Delta I_n &= I(t_k) - I(t_{k-1}) \end{aligned} \right. \end{aligned} \quad (23)$$

When visualizing and analyzing results, it is useful to know the SoC and SoH. The D2RC does not use these states for modelling or fitting. SoC quantifies the remaining charge q in the cell relative to the maximum charge capacity of the cell Q_m , given by

$$SoC = \frac{q}{Q_m} \quad (24)$$

The capacity Q_m decreases as the cell degrades. SoH is defined as the normalized maximum capacity, or Q_m relative to its initial value,

$$SoH = \frac{Q_m}{Q_{m0}} \quad (25)$$

Values for Q_m and q are obtained from coulomb counting. Processing for SoC and SoH is performed offline, and is used only for providing a reference when plotting results.

3.2. Parameter identification

Parameter identification is performed with constrained function minimization. This is implemented here using MATLAB-based global optimization for non-convex functions [30], though

many other approaches have been studied [31]. The problem statement is given by

$$\begin{aligned} & \text{minimize} && f(\theta) \\ & \text{subject to} && \theta \succ 0 \end{aligned} \quad (26)$$

We define

$$\begin{aligned} f(\theta) &= \|r\|_2^2 + a\|r'\|_2^2 \\ r(k) &= y(t_k) - \hat{y}(t_k, \theta) \\ r'(k) &= r(k+1) - r(k) \\ \theta &= (R_0 \quad R_1 \quad R_2 \quad C_1 \quad C_2 \quad A_D)^T \end{aligned} \quad (27)$$

for all $k = 1, \dots, K$, where there K available data points, y and \hat{y} are the observed and predicted data, θ is the parameter vector, and we set the weighting $a = 1$. The objective function f is composed of two terms: the sum of squared residuals (SSR) $\|r\|_2^2$ and the sum of squared residual differences (SSRD) $\|r'\|_2^2$. The SSR term minimizes the total tracking error. The SSRD term performs quadratic smoothing to avoid large spikes in prediction and increase agreement in curvature between the observed and predicted data.

Since the OCV variation has no fitting parameters, the observed data is defined as

$$y(t) = V_{OC}(t) - V_o(t) \quad (28)$$

and the predicted data is given by

$$\hat{y}(t, \theta) = V_s(t) + V_{ct}(t) + V_D(t) \quad (29)$$

Data predictions are defined with the discrete-time expressions as derived in Section 2, represented in state-space form as

$$\begin{pmatrix} V_s(t_{k+1}) \\ V_{ct}(t_{k+1}) \\ V_D(t_{k+1}) \end{pmatrix} = \begin{pmatrix} R_0 i(t_{k+1}) \\ \sum_{n=1}^2 R_n \left(i_{Rn}(t_k) e^{-\frac{\Delta t}{\tau_n C_n}} + i(t_k) (1 - e^{-\frac{\Delta t}{\tau_n C_n}}) \right) \\ A_D \sum_{n=1}^{N_p} \Delta I_n \frac{\partial V_{OC}}{\partial S_0 C} \sqrt{H(t_k - t_n) (\Delta t + \psi_n^2(t_k))} \end{pmatrix} \quad (30)$$

with initial conditions of

$$\begin{aligned} V_s(0) &= R_0 i(0) \\ V_{ct}(0) &= 0 \\ V_D(0) &= 0 \end{aligned} \quad (31)$$

Optimization also requires an initialization of the parameter vector. This is accomplished with reasonable guesses of the expected magnitudes.

4. Simulated Data

4.1. Data simulation with a physics-based model

Simulated data is generated using a coupled agglomerate-scale and electrode-scale continuum PBM for an NMC cell, described in detail in [32, 33]. This is used to verify the physical relevance of the proposed diffusion element. The PBM is known to simulate a single capacitive effect, so the D1RC is used for ECM parameter estimation.

Internal cell states are defined as user inputs, so changes in cell behavior can be linked directly to the internal states. There are 3 states chosen for evaluation: agglomerate diffusivity D_{agg} , reaction constant k_{rxn} , and contact resistance R_c . Diffusivity governs the diffusion of lithium ions through the agglomerates due to concentration gradients. Reaction constant is directly proportional to exchange current density. Contact resistance is the resistance of the current collector. The selected internal states are summarized in Table 1. These specific states are chosen to cover the same overpotentials captured by the DNRC model. Each internal state is expected to correlate with a single electrochemical overpotential: diffusivity with diffusion, reaction constant with charge transfer, and contact resistance with the solution overpotential.

The PBM is used to generate 3 datasets with the simulated pulse protocol. In each dataset, one of the three states is varied whilst the others are kept constant. Like the experimental pulse protocol, the simulated voltage responses represent SoC levels from 0 to 1. The simulated data is shown in Figure 2.

As shown in equation 16, the proposed diffusion constant A_D can be used to directly estimate the true diffusivity when the internal material parameters are known. The apparent diffusivity \hat{D} is given by

$$\hat{D} = \frac{4\bar{a}_x}{\pi} \left(\frac{\beta v_M}{SFA_D} \right)^2 \quad (32)$$

where $\bar{a}_x = 5.67$ is the average experimental underestimation prefactor and $\beta = 1/0.55$. The value of \bar{a}_x is derived from the results in [33]. It represents the amount by which the physical assumptions used to derive A_D are known to underestimate \hat{D} in porous electrode systems. The value of β is the inverse of the maximum stoichiometric added lithium relative to NMC. The molar volume v_M of NMC is calculated using

$$v_M = \frac{M_{NMC}}{\rho_{NMC}} \quad (33)$$

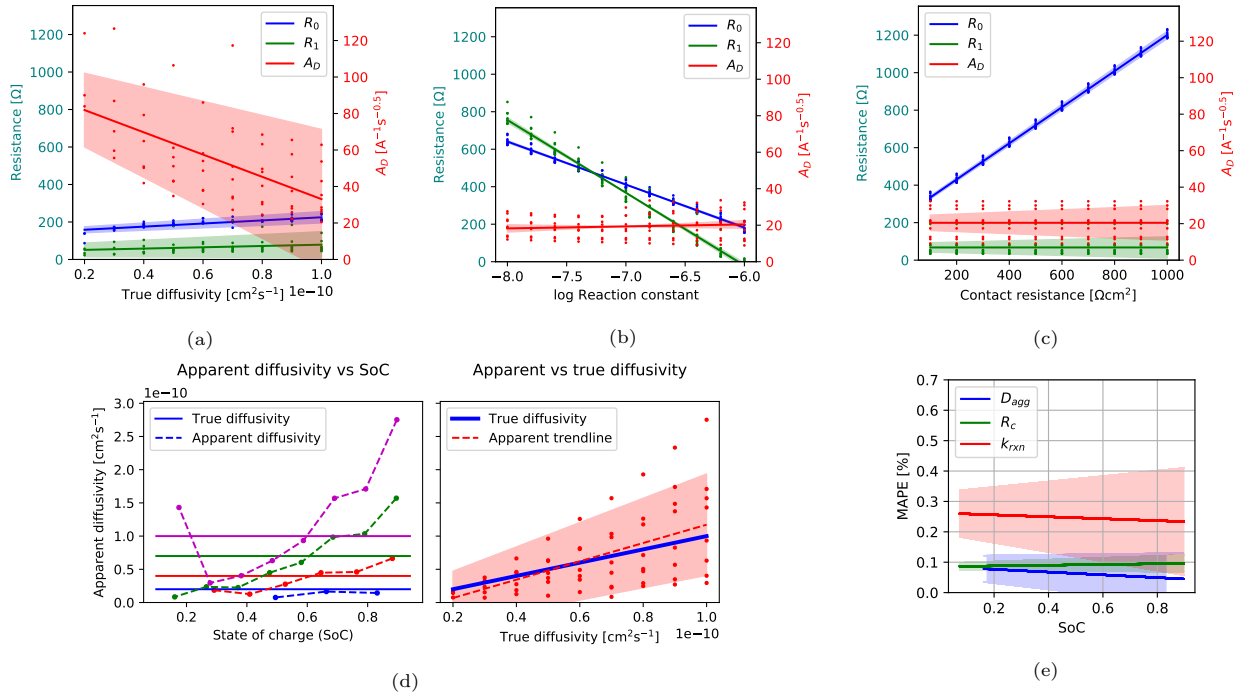


Figure 3: Variation of estimated DIRC parameters against (a) varying true diffusivity, (b) varying reaction constant, and (c) varying contact resistance; (d) Apparent diffusivity extracted from the DIRC model, plotted against SoC for selected values of true diffusivity (left), and plotted against true diffusivity (right); and (e) MAPE of DIRC voltage predictions

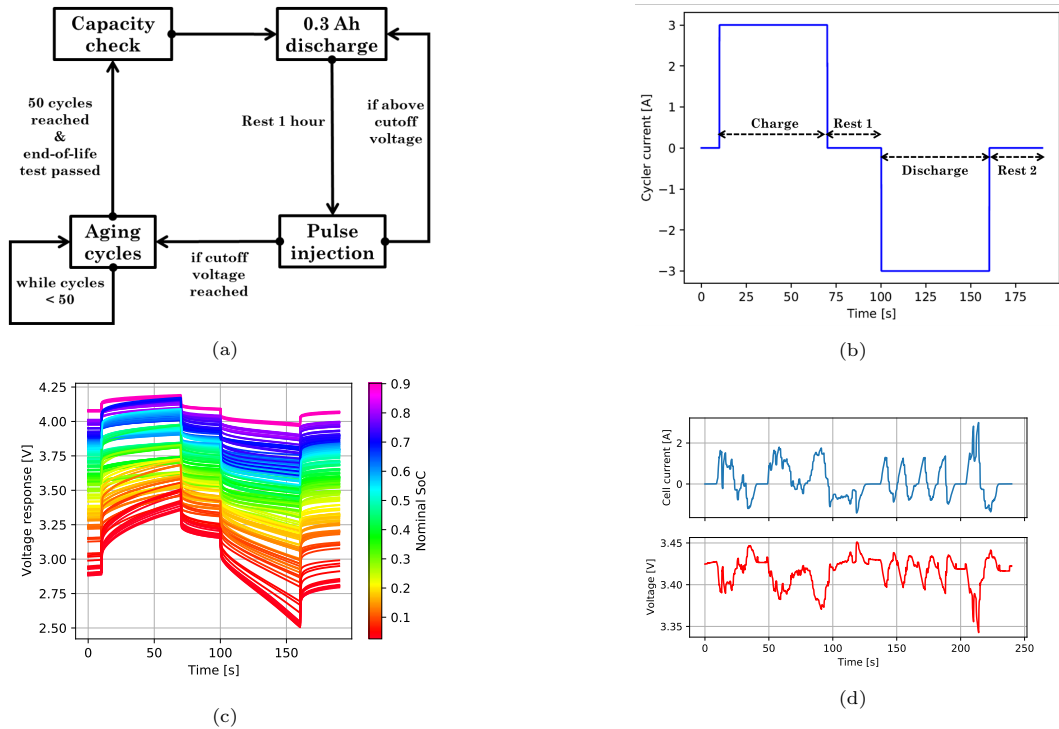


Figure 4: Figures for experimental data collection, with (a) Experimental pulse injection data acquisition procedure for various SoC and SoH, (b) Current pulse from cycler, (c) Voltage responses to pulse injection color-coded by SoC, and (d) Cell current and output voltage of drive cycle data

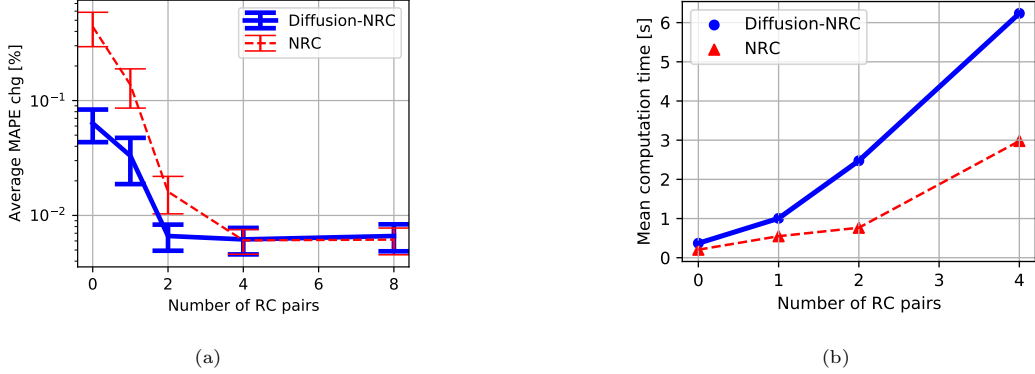


Figure 5: Comparison between proposed DNRC model and conventional NRC model for (a) average MAPE and (b) average computation time

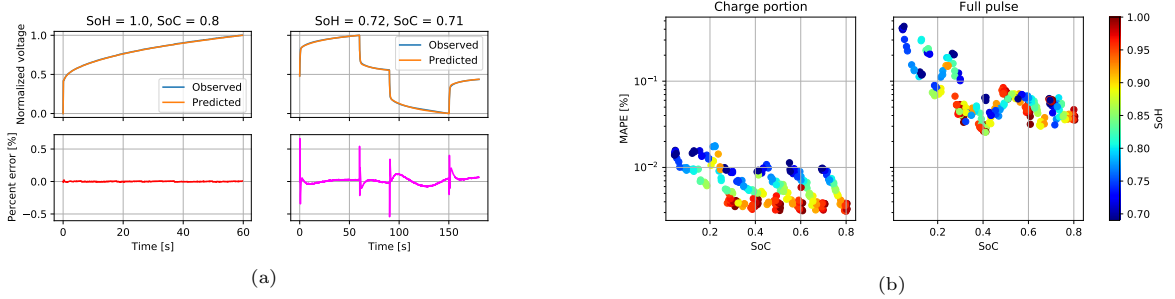


Figure 6: Voltage tracking and MAPE for unipolar and bipolar pulse, with (a) samples of observed and predicted voltage and (b) the D2RC MAPE

where $M_{\text{NMC}} = 96.46 \text{ gmol}^{-1}$ is the molar mass of NMC, and $\rho_{\text{NMC}} = 4.7 \text{ gcm}^{-3}$ is the density of NMC. The active surface area is given by

$$S = \frac{3\varepsilon_{AM}}{L_{agg}} v_e \quad (34)$$

where $\varepsilon_{AM} = 0.306$ is the volume fraction of active material, $L_{agg} = 1\mu\text{m}$ is the size of the agglomerate, and v_e is electrode volume, which varies with model parameters.

4.2. Comparison between physics-based model and proposed model

Results for the comparison between the PBM and the proposed D1RC model are shown in Figure 3, with 3 plots displaying the variation of D1RC parameters with internal PBM states, a plot of the apparent diffusivity extracted from the D1RC model, and a comparison of the MAPE of the voltage predictions. There is good agreement between the D1RC predicted voltage and the PBM generated voltage, with average MAPE below 0.5%, as shown in Figure 3e.

There are clear and distinct trends in the D1RC parameters for each dataset. When diffusivity is varied, correlation is strong with A_D but negligible with R_0 and R_1 . When the reaction constant is varied, correlation is strong with R_0 and R_1 but negligible with A_D . When contact resistance is varied, correlation is very strong with R_0 , and negligible with R_1 and A_D .

The results in Figure 3 show that the effects of individual cell states can be captured by the D1RC model. As expected, the novel diffusion element is most correlated with the varying diffusivity, and R_0 is most correlated with the contact resistance. Varying the reaction constant, however, has more complex effects on the voltage response that cannot be captured by a single circuit element. It is correlated with both the charge transfer and solution overpotentials.

Apparent diffusivity \hat{D} is compared with true diffusivity D_{agg} in Figure 3d, plotted against both SoC and D_{agg} . Unlike D_{agg} , which does not vary with SoC, \hat{D} does vary with SoC. This may be due to

Table 1: Internal cell states varied in physics-based model simulations

Symbol	Meaning	Range	Units
D_{agg}	Agglomerate diffusivity	$\{0.2, 0.3, \dots, 1\} \times 10^{-10}$	$[\text{cm}^2 \text{s}^{-1}]$
k_{rxn}	Reaction constant	$10^{\{-8, -7.8, \dots, -6\}}$	$[\text{mol}^{-0.5} \text{cm}^{-0.5} \text{s}^{-1}]$
R_c	Contact resistance	$\{0.1, 0.2, \dots, 1\}$	$[\text{k}\Omega \text{cm}^2]$

Table 2: Cell characteristics

Characteristic	Value	Units
Cell chemistry	NCA	$[-]$
Nominal capacity	3000	$[\text{mAh}]$
Cut-off voltage	2.5	$[\text{V}]$
Cut-off current	150	$[\text{mA}]$
Max charge voltage	4.2	$[\text{V}]$
Peak charging current	4	$[\text{A}]$
Peak discharge current	15	$[\text{A}]$

SoC-varying states in the PBM, such as initial concentration, that are not accounted for by elements in the D1RC model. The trend line of \hat{D} is highly correlated with D_{agg} , showing good agreement between the apparent and true diffusivities.

5. Experimental Data

5.1. Data collection

Data was collected using 3 lithium nickel cobalt aluminum (NCA) oxide cells (Samsung INR18650-30Q). NCA cells have desirable performance, but require additional safety considerations [34]. Cells are cycled simultaneously and under the same conditions to reduce the effects of individuality. Cell characteristics are summarized in Table 2.

Cells were cycled using the Neware BTS4000 series 5V6A cycler, held at 25°C and standard pressure. Cell voltage and cycler current are monitored at 10 Hz.

Experimental data is collected using two cycling procedures: pulse injection at various SoC and SoH, and an urban dynamometer driving schedule (UDDS) drive cycle. Pulse injection data, shown in Figures 4b and 4c is used to evaluate the ECM under different charging and degradation levels for large step changes in current. Drive cycle data, shown in Figure 4d, is used to evaluate the ECM for a pseudo-randomly varying input current sequence. The two datasets aim to isolate the effects of internal state variation and input signal variation on estimation accuracy.

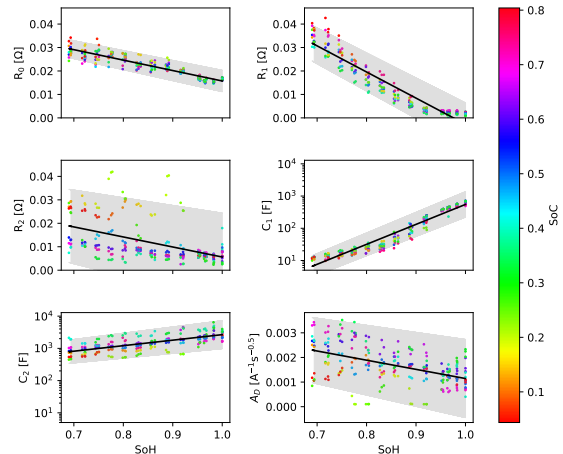


Figure 7: Evolution of estimated D2RC parameters with SoH for charge portion of experimental data (individual values and trend line)

Cycling procedure for pulse injection is illustrated in Figure 4a. The capacity check is performed with a 0.1 C-rate constant current (CC) discharge from full. This is used to determine the SoH of the cell, which ranges from 0.69 to 1. After the cell is recharged using CC and constant voltage (CV), various SoC levels ranging from 0.5 to 0.8 are achieved using a 0.3 Ah discharge. Degradation is performed with 50 charge/discharge cycles at 1 C-rate. Pulses are applied to the cell after a 1 hour rest period. Positive cycler current indicates current into the cell.

5.2. Results for pulse injection data

DNRC model performance is first compared with conventional NRC model performance in Figure 5. The average mean absolute percent error (MAPE) and parameter estimation time (computation time) for the charge portions of the pulses are plotted against the number of RC-pairs, with standard deviation shown as error bars. The 0RC model only uses R_0 , while the D0RC model uses R_0 and the proposed element A_D .

As shown in Figure 5a, addition of the proposed diffusion element improves estimation accuracy un-

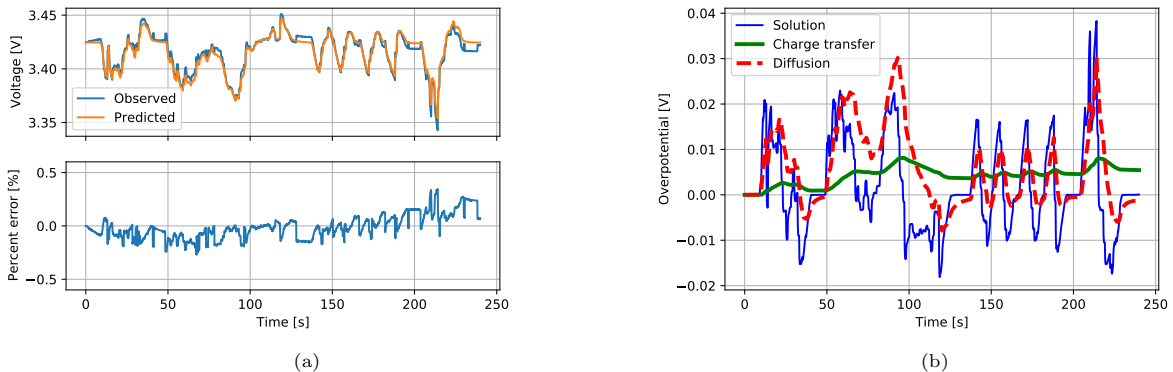


Figure 8: Results for experimental drive cycle data, with (a) percent error of predicted voltage and (b) predicted overpotential voltages

til 4 RC-pairs are used. This suggests that it is more efficient at modelling cell behavior compared to RC-pairs. Thus the proposed D2RC model, which uses 6 parameters, is comparable in accuracy to the conventional 4RC model, which uses 9 parameters. The reduction of 3 fitting parameters to achieve similar accuracies improves model interpretability. Although the diffusion element demands more computation time using the same number of RC-pairs, the D2RC model is slightly faster than 4RC, as can be seen in Figure 5b. Therefore D2RC strikes a balance between low error and high interpretability, and demonstrates a wholistic improvement over conventional NRC models.

Voltage tracking using the D2RC model for the unipolar and bipolar pulse is shown in Figures 6a for various SoH and SoC. The MAPE for all 234 responses is shown in Figure 6b. MAPE is below 0.02% for the unipolar pulse, and below 0.5% for the bipolar pulse. Error increases for bipolar pulse estimation at low SoC and low SoH. This may be attributed to OCV variation or degradation dynamics not captured by the estimated OCV or the model itself. Error also spikes during step changes, which may affect the constant-current estimation.

Estimated parameters of the D2RC model for the unipolar pulse are shown in Figure 7. There are clear trends as the cell degrades and SoH decreases. Resistances and the diffusion constant increase with degradation, while capacitances decrease. This suggests that the model parameters can be used to track degradation. For cells cycled under different conditions, the trends in the parameters may be similarly distinct.

5.3. Results for drive cycle data

Results for a selection of drive cycle data are shown in Figure 8a. The absolute percent error is below 0.4%, showing that the D2RC model can accurately track voltage for an arbitrary input signal. The physical relevance of the D2RC model also allows the dominant overpotentials to be identified over time, plotted in Figure 8b. It can be seen that the solution and diffusion overpotentials are dominant, which is supported by observations in [35].

5.4. Limitations

There are limitations to the DNRC model, as suggested earlier. For tracking voltage with large variation and time horizons longer than 5 minutes, the model as formulated would require a large number of diffusion states arising from the number of step changes in the interval. It is known, however, that the effects of multiple diffusion steps can ‘cancel’ each other over time, meaning that it is not necessary to retain all the states. The model can be therefore be modified to use a fixed time horizon or limit on the number of diffusion states. This would reduce the computational burden with negligible effect on accuracy.

6. Conclusion

The DNRC ECM captures electrochemical overpotential behavior, including solution voltage, charge transfer, and diffusion, using a series resistor, RC-pairs, and a novel diffusion element. The DNRC ECM can be implemented in discrete-time

state-space form, allowing for real-time estimation. Three-fold validation with experimental and PBM-simulated data shows that D2RC ECM parameters not only yield high accuracy predictions, but are also linked to internal cell states.

The D2RC ECM may provide a simple and fast method to track battery degradation processes using time-domain data. With further research, the D2RC model may be able to show that different battery cycling conditions, such as extreme temperatures, high C-rates, or extreme SoC, yield different ‘signatures’ in the parameter evolution plots. Combined with fast and accurate SoH estimation techniques, the D2RC ECM could then be used in the BMS to actively adjust battery pack performance to reduce degradation [36] thus allowing for new control methods.

7. Acknowledgements

This research was undertaken, in part, through funding from the Columbia University Data Science Institute (DSI) Seed Fund Program. We also thank Robert C. Mohr for contributions to the experimental setup and Zeyu Hui for additional support.

References

- [1] T. Kim, W. Song, D. Son, L. K. Ono, Y. Qi, Lithium-ion batteries: outlook on present, future, and hybridized technologies, *Journal of Materials Chemistry A* 7 (2019) 2942–2964.
- [2] Y. Wang, J. Tian, Z. Sun, L. Wang, R. Xu, M. Li, Z. Chen, A comprehensive review of battery modeling and state estimation approaches for advanced battery management systems, *Renewable and Sustainable Energy Reviews* 131 (2020).
- [3] L. Lu, X. Han, J. Li, J. Hua, M. Ouyang, A review on the key issues for lithium-ion battery management in electric vehicles, *Journal of Power Sources* 226 (2014) 272–288.
- [4] W. Waag, C. Fleischer, D. U. Sauer, Critical review of the methods for monitoring of lithium-ion batteries in electric and hybrid vehicles, *Journal of Power Sources* 258 (2014) 321–339.
- [5] F. Saidani, F. X. Hutter, R. G. Scurtu, W. Braunwarth, J. N. Burghartz, Lithium-ion battery models: a comparative study and a model-based powerline communication, *Advances in Radio Science* 15 (2017) 83–91.
- [6] J. Li, D. Wang, L. Deng, Z. Cui, C. Lyu, L. Wang, M. Pecht, Aging modes analysis and physical parameter identification based on a simplified electrochemical model for lithium-ion batteries, *Journal of Energy Storage* 31 (2020).
- [7] Z. Ma, Z. Wang, R. Xiong, J. Jiang, A mechanism identification model based state-of-health diagnosis of lithium-ion batteries for energy storage applications, *Journal of Cleaner Production* 193 (2018) 379–390.
- [8] Y. Li, M. Vilathgamuwa, S. S. Choi, T. W. Farrell, N. T. Tran, J. Teague, Development of a degradation-conscious physics-based lithium-ion battery model for use in power system planning studies, *Applied Energy* 248 (2019) 512–525.
- [9] A. Smiley, G. L. Plett, An adaptive physics-based reduced-order model of an aged lithium-ion cell, selected using an interacting multiple-model kalman filter, *Journal of Energy Storage* 19 (2018) 120–134.
- [10] S. G. Marquis, R. Timms, V. Sulzer, C. P. Please, S. J. Chapman, A suite of reduced-order models of a single-layer lithium-ion pouch cell, *Journal of the Electrochemical Society* 167 (2020).
- [11] C. Chen, R. Xiong, W. Shen, F. Sun, State-of-charge estimation of lithium-ion battery using an improved neural network model and extended kalman filter, *Journal of Cleaner Production* 234 (2019) 1153–1164.
- [12] K. A. Severson, P. M. Attia, N. Jin, N. Perkins, B. Jiang, Z. Yang, M. H. Chen, M. Aykol, P. K. Her-ring, D. Fraggedakis, M. Z. Bazant, S. J. Harris, W. C. Chueh, R. D. Braatz, Data-driven prediction of battery cycle life before capacity degradation, *Nature Energy* 4 (2019) 383–391.
- [13] N. Meddings, M. Heinrich, F. Overney, J. Lee, V. Ruiz, E. Napolitano, S. Seitz, G. Hinds, R. Raccichini, M. Gaberscek, J. Park, Application of electrochemical impedance spectroscopy to commercial li-ion cells: A review, *Journal of Power Sources* 480 (2020).
- [14] W. Choi, H. Shin, J. M. Kim, J. Choi, W. Yoon, Modeling and applications of electrochemical impedance spectroscopy (EIS) for lithium-ion batteries, *Journal of Electrochemical Science and Technology* 11 (2020) 1–13.
- [15] Z. Guo, X. Qiu, G. Hou, B. Y. Liaw, C. Zhang, State of health estimation for lithium ion batteries based on charging curves, *Journal of Power Sources* 249 (2014) 457–462.
- [16] U. Westerhoff, K. Kurbach, F. Lienesch, M. Kurrat, Analysis of lithium-ion battery models based on electrochemical impedance spectroscopy, *Energy Technology* 4 (2016) 1620–1630.
- [17] S. M. M. Alavi, C. R. Birkl, D. A. Howey, Time-domain fitting of battery electrochemical impedance models, *Journal of Power Sources* 288 (2015) 345–352.
- [18] A. Nasser-Eddine, B. Huard, J. D. Gabano, T. Poinot, S. Martemianov, A. Thomas, Fast time domain identification of electrochemical systems at low frequencies using fractional modeling, *Journal of Electroanalytical Chemistry* 862 (2020) 345–352.
- [19] J. Tian, R. Xiong, W. Shen, F. Sun, Fractional order battery modelling methodologies for electric vehicle applications: Recent advances and perspectives, *Science China Technological Sciences* 63 (2020).
- [20] S. Gantenbein, M. Weiss, E. Ivers-Tiffé, Impedance based time-domain modeling of lithium-ion batteries: Part i, *Journal of Power Sources* 379 (2018) 317–327.
- [21] U. Krewer, F. Roder, E. Harinath, R. D. Braatz, B. Bedurftig, R. Findeisen, Review—dynamic models of li-ion batteries for diagnosis and operation: A review and perspective, *Journal of the Electrochemical Society* 165 (2018) A3656–A3673.
- [22] C. Brivio, V. Musolino, M. Merlo, C. Ballif, A physically-based electrical model for lithium-ion cells, *IEEE Transactions on Energy Conversion* 34 (2019).
- [23] K. S. Cole, R. H. Cole, Dispersion and absorption in

- dielectrics I. alternating current characteristics, *The Journal of Chemical Physics* 9 (1941).
- [24] Q. Yu, R. Xiong, C. Lin, A comparative study on open circuit voltage models for lithium-ion batteries, *Chinese Journal of Mechanical Engineering* 31 (2018).
- [25] R. Zhang, B. Xia, B. Li, L. Cao, Y. Lai, W. Zhang, H. Wang, W. Wang, M. Wang, A study on the open circuit voltage and state of charge characterization of high capacity lithium-ion battery under different temperature, *Energies* 11 (2018).
- [26] X. Chen, H. Lei, R. Xiong, W. Shen, R. Yang, A novel approach to reconstruct open circuit voltage for state of charge estimation of lithium ion batteries in electric vehicles, *Applied Energy* 255 (2019).
- [27] J. Li, N. Lotfi, R. G. Landers, J. Park, A single particle model for lithium-ion batteries with electrolyte and stress-enhanced diffusion physics, *Journal of The Electrochemical Society* 164 (2017).
- [28] W. Ai, L. Kraft, J. Sturm, A. Jossen, B. Wu, Electrochemical thermal-mechanical modelling of stress inhomogeneity in lithium-ion pouch cells, *Journal of The Electrochemical Society* 167 (2019).
- [29] W. Weppner, R. A. Huggins, Determination of the kinetic parameters of mixed-conducting electrodes and application to the system Li_3Sb , *Journal of the Electrochemical Society* 124 (1977) 1569–1578.
- [30] Z. Ugray, L. Lasdon, J. Plummer, F. Glover, J. Kelly, R. Marti, Scatter search and local nlp solvers: A multistart framework for global optimization, *INFORMS Journal on Computing* 19 (2007) 328–340.
- [31] I. P. Androulakis, C. D. Maranas, C. A. Floudas, abb: A global optimization method for general constrained nonconvex problems, *Journal of Global Optimization* 7 (1995) 337–363.
- [32] N. W. Brady, Q. Zhang, A. Bruck, D. C. Bock, C. A. Gould, A. C. Marschilok, K. Takeuchi, E. Takeuchi, A. C. West, Operando study of LiV_3O_8 cathode: Coupling EDXRD measurements to simulations, *Journal of the Electrochemical Society* 165 (2018) A371–A379.
- [33] Z. Hui, K. S. Mayilvahanan, Y. Yang, A. C. West, Determining the length scale of transport impedances in li-ion electrodes: $\text{Li}(\text{Ni}_{0.33}\text{Mn}_{0.33}\text{Co}_{0.33})\text{O}_2$, *Journal of the Electrochemical Society* 167 (2020).
- [34] Y. Miao, P. Hynan, A. Jouanne, A. Yokochi, Current Li-Ion battery technologies in electric vehicles and opportunities for advancements, *Energies* 12 (2019).
- [35] V. J. Ovejas, A. Cuadras, State of charge dependency of the overvoltage generated in commercial Li-ion cells, *Journal of Power Sources* 418 (2019) 176–185.
- [36] M. M. Kabir, D. E. Demirocak, Degradation mechanisms in Li-ion batteries: a state-of-the-art review, *International Journal of Energy Research* 41 (2017) 196–1986.